nature geoscience

ARTICLES

https://doi.org/10.1038/s41561-020-0636-8

Longwave radiative effect of the cloud twilight zone

Eshkol Eytan[1], Ilan Koren[1]✉, Orit Altaratz[1], Alexander B. Kostinski[2] and Ayala Ronen[3]

Clouds play a key role in Earth's radiation budget, covering more than 50% of the planet. However, the binary delineation of cloudy and clear sky is not clearly defined due to the presence of a transitionary zone, known as the cloud twilight zone, consisting of liquid droplets and humidified to dry aerosols. The twilight zone is an inherent component of cloud fields, yet its influence on longwave-infrared radiation remains unknown. Here we analyse spectral data from global satellite observations of shallow cloud fields over the ocean to estimate a lower bound on the twilight zone's effect on longwave radiation. We find that the average longwave radiative effect of the twilight zone is ~0.75 W m^{-2}, which is equivalent to the radiative forcing from increasing atmospheric CO_2 by 75 ppm. We also find that the twilight zone in the longwave occupies over 60% of the apparent clear sky within the analysed low-level cloud fields. As low-level clouds are relatively warm, the overall longwave radiative contribution from the twilight zone is likely to be higher. We suggest that the twilight zone needs to be accounted for to accurately quantify cloud radiative effects and close the global energy budget.

Clouds are a major component of Earth's hydrological cycle and energy budget. Their anthropogenic radiative forcing (through aerosol–cloud interactions) is considered to be highly uncertain, ranging from counteracting CO_2 warming to a negligible effect (IPCC 2013)[1]. In general, cloud feedback to a warmer planet is assumed to be positive (warming), although it is considered highly uncertain[2–4]. Clouds' radiative effect (CRE) can be separated into cooling and warming[5–7] due to their interactions with both shortwave (solar) and longwave-infrared radiation (which is emitted by Earth). The CRE in the solar radiation spectrum is mainly the reflection of radiation back to space (cooling effect of the Earth; CRE < 0). Simultaneously, clouds block longwave-infrared radiation from escaping to space (warming effect; CRE > 0) by absorbing the upwelling flux from below and re-emitting a fraction out to space that is proportional to their colder temperature. Clouds' microphysical and macrophysical properties determine their net radiative effect, which varies greatly for different cloud types, and in both time and space. Low-level clouds can be almost opaque to solar radiation but have only a small deviation from the surface temperature, and so their net CRE is cooling (negative). By contrast, cirrus clouds are likely to have a positive CRE, as they are semitransparent to solar radiation but are much colder than the surface[6].

It is common to calculate the CRE of a specific domain as the difference between the radiative fluxes from clear and cloudy pixels multiplied by the domain's cloud fraction[8,9]. However, to correctly determine CRE, one has to accurately determine clouds' coverage (cloud fraction) and be able to clearly distinguish clear sky from cloudy. This demands a determination of clouds' boundaries, which is an elusive parameter that depends on the observation technique and chosen thresholds[10]. It has been shown that a main component of the sky cannot be defined as cloudy or clear; this component was named the clouds' 'twilight zone'[11] or 'albedo continuum'[12]. A metric of distance from the nearest cloud (DFNC) was used[11] to show that the solar reflectance values are inversely correlated to this distance. Satellite and ground observations have shown that the twilight zone can be detected up to 30 km away from clouds and have an e-fold of 10 km. Other studies have shown that the twilight fraction of the so-called 'clear skies' is more than 50% (refs. [13,14]). The twilight zone has been explored using solar radiation measurements, and three main components have been suggested to explain the observations: (1) undetectable clouds: subpixel clouds[15] and optically thin clouds[16,17] (small/dissipating/forming clouds or cloud fragments); (b) three-dimensional effect: secondary illumination of aerosols by photons escaping from the sides of clouds[18,19]; (c) humidified aerosols: enlargement of the cross section of scattering aerosols by water uptake[14,20,21]. These components in a cloud field are created by different physical mechanisms; thus, it is important to be able to distinguish them for process-level understanding and direct modelling of the twilight zone[22].

The extent of the twilight zone and its components are properties of the cloud field and depend on the thermodynamic and microphysical properties of the field, such as the relative humidity, stability and aerosol properties. The distance from the nearest cloud's approach is used as a statistical measure for the likelihood to find twilight components. This highlights the duality of the twilight concept; each component, (for example, small clouds, haze pockets or secondary illumination by clouds) is related to different physical processes and can be well constrained in space, but the twilight region average properties often show a continuum.

Here we explore the twilight zone in the longwave part of the spectrum (TLW) by analysing warm cloud fields on a global scale. The data were acquired by the moderate-resolution imaging spectrometer (MODIS) on board Aqua. We used the longwave atmospheric window to calculate a lower limit of the clouds' TLW warming effect. In addition, our results suggest possible errors in remote-sensing retrievals caused by the TLW.

Radiative properties of the TLW

Figure 1 presents a cumulus cloud field (over the Indian Ocean) in true colours (Fig. 1a) and in 11 μm (Fig. 1b) brightness temperature. Figure 1c is a zoom-in image of the red square marked in Fig. 1b, with masked clouds (marked in white), and marked locations of low brightness temperature within the clouds' TLW that demonstrate different structures: (1) a thin cloud 'halo' is shown within the solid

[1]Department of Earth and Planetary Science, The Weizmann Institute of Science, Rehovot, Israel. [2]Physics Department, Michigan Technological University, Houghton, MI, USA. [3]Department of Environmental Physics, Israel Institute for Biological Research, Nes-Ziona, Israel. ✉e-mail: ilan.koren@weizmann.ac.il

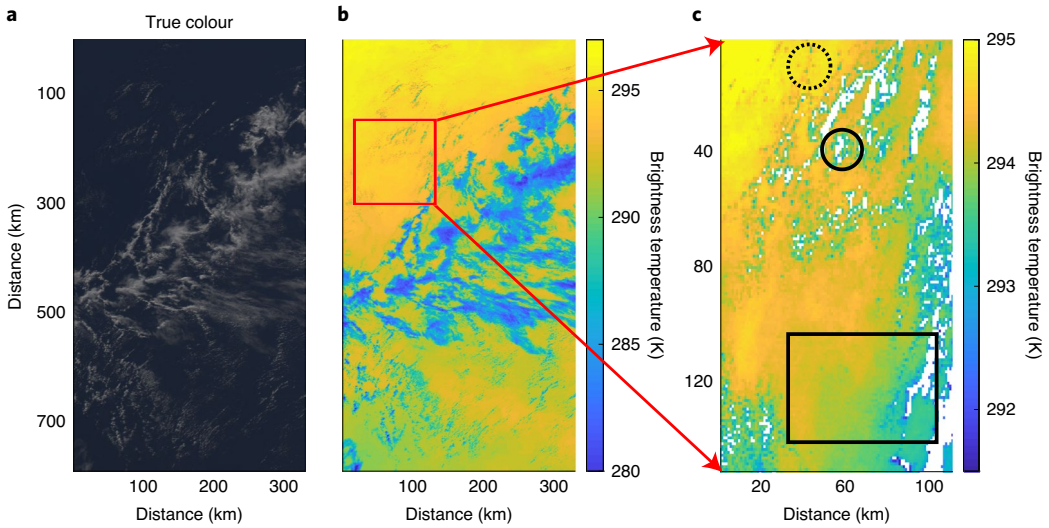

Fig. 1 | Clouds' TLW. An example of a scene (Indian Ocean, 1 km resolution, 21 June 2014, centre of granule at 24° S, 73° E). **a**, MODIS/Aqua level 1B true colour image of the scene. **b**, MODIS/Aqua level 1B 11 μm brightness temperature (K). **c**, A zoom-in on the red box in **b** with clouds masked in white. The TLW signature is shown as reduced brightness temperatures in what is defined as a clear atmosphere over the warm ocean. The structures present a halo around the clouds (solid circle), long-distance gradients from clear sky to cloud (square) and isolated pockets of reduced temperatures (dashed circle).

circle; (2) weaker gradients around clouds are presented within the square; (3) small isolated pockets are marked by the dashed circle. The causes of the observed TLW are expected to differ from those in the solar (shortwave) radiation due to the different refractive indices and size parameters (particle-to-wave-length ratio). The absorption by liquid particles and water vapour is negligible in the visible but strong in the longwave. While liquid water strongly absorbs throughout the entire longwave part of the spectrum, water vapour has an absorption minimum in the longwave window (8–12 μm). There is little absorption in the longwave atmospheric window by other greenhouse gases, and it is therefore used for remote sensing of surface temperature and water-vapour concentration[23]. For a given aerosol concentration, the average cloud droplet size is proportional to the amount of liquid water in a volume (liquid water content; g m^{-3}) (refs. [16,24]). Since the twilight zone has been shown to contain small (or thin) clouds and humidified aerosols, it mostly consists of particle sizes that range between submicron (humidified aerosols) and a few microns (small droplets)[15]. We used a radiation transfer model[25] and Mie theory calculations in the longwave[26] to show that for this range of sizes, longwave scattering is minor, and hence the three-dimensional effect (which is a scattering mechanism) can be neglected (Supplementary Fig. 1). It is also shown that the absorption by growing submicron particles cannot explain the whole observed effect of the TLW (section 1 of the Supplementary Information). Therefore, the clouds' twilight zone signature in the longwave is likely to be controlled by the elevated water-vapour concentrations, undetectable clouds and haze particles in the order of 1 μm. Figure 2a shows the solar and longwave signals as a function of the DFNC for the scene shown in Fig. 1. The calculation of the DFNC presented here used MODIS's cloud mask product (MYD35, quality assurance 00). The known decay of reflectance in the shortwave is observed[11,27]. In addition, it is shown that the longwave brightness temperature increases with DFNC; this metric will be used to define the TLW's extent and properties.

The TLW signature can also be shown using sea surface temperature (SST) retrievals, obtained here from the well-validated MODIS SST product[28,29]. Figure 2b shows the deviation of a snapshot-calculated SST (for the good accuracy level) from the 8-day SST product (blue curve) as a function of DFNC (see section 3 of the Supplementary Information). In this example, the good and

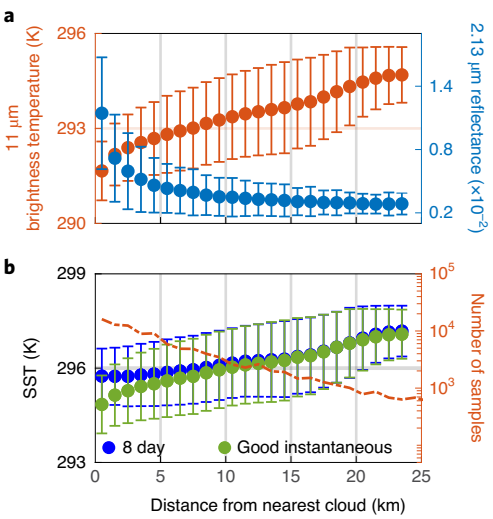

Fig. 2 | Twilight zone signal as a function of DFNC. a, The mean and standard deviation for brightness temperature of 11 μm (red) and reflectance of 2.13 μm (blue) for the warm cumulus field seen in Fig. 1 versus DFNC. **b**, MODIS SST product comparison; 8-day level 3 SST (blue) and the instantaneous level 2 good quality assurance (green) versus DFNC. The number of samples in each DFNC bin is given by the red curve. Error bars represent the standard deviation; the standard error in both panels is smaller than the size of the dots due to the large sample size. The standard deviation represents the uncertainty due to the spread of samples and does not account for the errors of the instruments or retrievals.

best qualities aligned well together (the best-quality pixels' number was much smaller near clouds); therefore, we present only the good-quality pixels. Some images showed deviation also between the two quality flags. The SST calculation assumes a cloud-free radiation path and includes spectral analysis in the atmospheric window to correct for the water-vapour attenuation of radiation[23]. Thus, only pixels that pass the detailed cloud-recognition algorithm (MODIS cloud mask in this case)[30] and are recognized as cloud-free

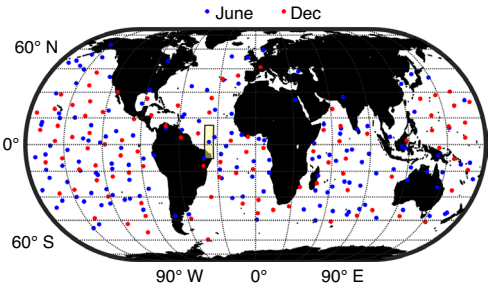

Fig. 3 | Global distribution of samples. Global distribution of 253 sampled granules by AQUA/MODIS during 6 days (21–23 June 2014 and 21–23 December 2014), shown in blue and red dots for June and December, respectively. Each point represents the centre of an analysed granule. The yellow polygon marks the analysed part of the granule, as defined by viewing angles of ±15°. Within it, only areas that met all other criteria were analysed.

are used for SST retrieval. This makes the SST estimations sensitive to undetected clouds. The uncertainty that the TLW can bring into SST retrievals is discussed in the section 4 of the Supplementary Information. There we suggest that a major cause of error in the SST estimation is unaccounted clouds/haze or errors in the estimations of water-vapour concentrations.

The warming radiative effect of the TLW

Six days of a global dataset of warm cloud fields over the oceans were used from 60° S to 60° N. This consists of a dataset of 253 granules of MODIS (Fig. 3 shows the centre of each granule), which held a total area of 56.8×10^6 km^2 (11% of Earth's surface) of warm cloud fields that met the analysis' criteria (more details in Methods). These were analysed to estimate the radiative effect in the longwave of the twilight zone (TLW RE).

To minimize the effect of assumptions and radiative transfer model sensitivities, we chose to bound the RE from below by adopting an underestimating approach that provides the lower limit to the TLW RE. The characteristic temperatures of warm shallow convective clouds are close to the SST below them (small contrast); thus, their weaker effect can be used to estimate the lower bound of the global effect. Moreover, the estimations of the energy-flux differences in this work were performed only in the longwave atmospheric window spectral range, which represents part of the energy emitted by a blackbody at Earth's temperatures. The RE of an atmospheric column was calculated as the difference between the upwelling radiation emitted by the surface and the radiation emitted at the top of the atmosphere (explained in Methods). Figure 4a shows the decay of the atmospheric RE as a function of DFNC for the example scene (Fig. 1). The extent of the TLW is defined here as the point where the decay is close to saturation. Accordingly, the far-field (clear sky) RE is taken as the mean of all pixels with DFNC larger than that extent. Figure 4b shows the distribution of RE values of all cloudy pixels (blue) and of all the pixels located at $1<\mathrm{DFNC}\leq2$ km (orange). The figure shows the inherent paradox of the twilight zone: an overlap of the signal of cloudy and clear pixels. Figure 4c presents distributions of RE for different sets of pixels with different DFNC. As we go farther away from the clouds, the mean RE decreases, and the right tail of the distribution shrinks (see decrease in standard deviation in Fig. 4a).

Figure 5a shows the contribution of each DFNC bin to the total effect, as averaged for the 6-day dataset. The effective extent of the TLW for each case was defined as the distance in which the accumulated contribution reached 90% of the total effect (the mean for all cases is denoted here by the shaded area). The box plot on the top left presents the total effect for all cases. Although a few cases

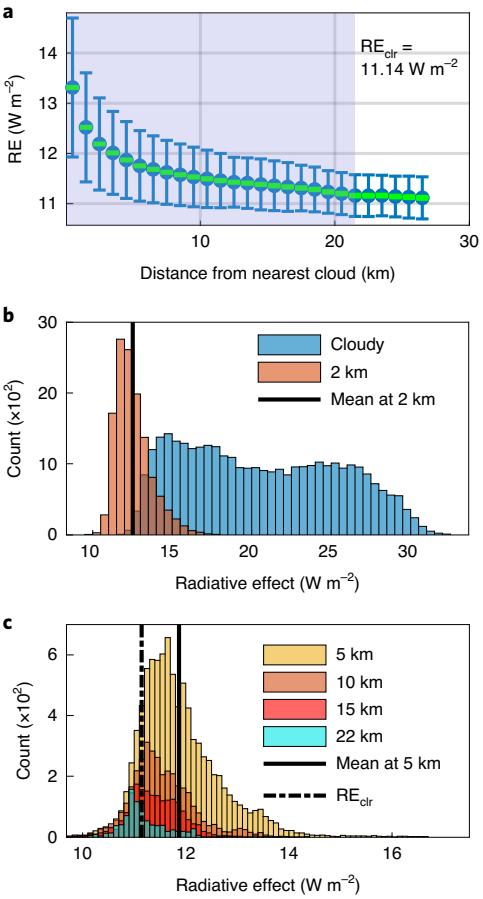

Fig. 4 | The TLW RE. a, The atmospheric radiative effect (W m^{-2}) for the example scene (Fig. 1) versus DFNC. The error bars mark the standard deviation, and the standard errors are represented by the vertical length of the green boxes inside the dots. The shaded area marks the TLW extent. **b**, The RE distribution of all cloudy (blue) and near-cloudy (orange; $1<\mathrm{DFNC}\leq2$) pixels. The vertical black line represents the mean of the distributions for DFNC of 2 km. **c**, The RE distributions (similar to the ones presented in **b**) but for longer distances from clouds (5, 10, 15 and 22 km). Vertical black lines are similar to **b** for 5 km (dashed) and mean clear-sky effect (RE_{clr}; solid). The means correspond to the dots presented in **a**; the medians are not shown since their difference from the mean is less than 0.1 W m^{-2}.

had a cooling (negative) effect (see section 7 of the Supplementary Information), almost 75% of the data had an effect larger than 0.5 W m^{-2}, with a mean and median around 0.75 W m^{-2}. Quantifying the area coverage of the twilight zone within the cloud field is of great importance. Blue dots in Fig. 5b show the mean area covered by each DFNC bin. The mean TLW extent and effective extent are marked by the light and dark shaded areas, respectively. The green dots represent the cumulative distribution of the area coverage out of the 'clear sky' (non-cloudy). This shows that the effective extent by itself captures more than 60% of the non-cloudy sky in the cloud field.

How sensitive is the TLW RE to the cloud-detection criteria? Since part of the TLW effect can be attributed to undetectable clouds, and the metric that we used is defined by distance from the clouds' edge, we can expect that the cloud mask will impact the magnitude of the effect. Therefore, we tested the sensitivity of the results to the cloud mask by performing an additional analysis using a different cloud mask of MODIS, which is used for clear-sky applications (Supplementary Fig. 3). This is a more conservative mask[31], which

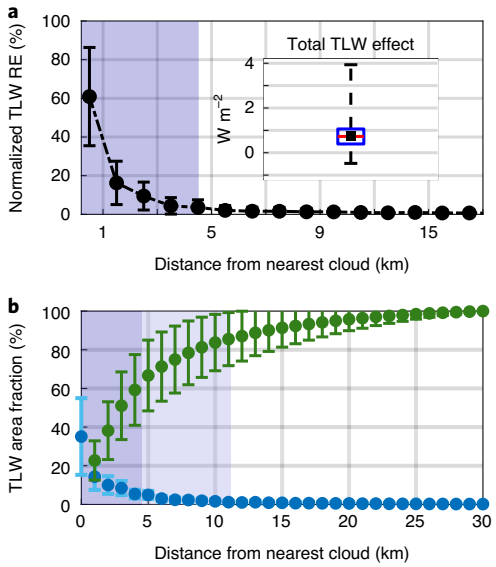

Fig. 5 | Global analysis results. a, The mean contribution of each DFNC bin to the total effect. Error bars represent the standard deviation. The shaded area represents the mean effective extent, where 90% of the effect occurs. The box plot on the top right shows the distribution of the total effect for all samples: black square for mean, red line for the median, blue box for 25 and 75 percentiles, and dashed error bars for minimum and maximum values (the four lowest outliers were excluded; for the full box plot see Supplementary Fig. 7). **b**, Mean area coverage of each DFNC bin in blue dots (for example, mean cloud cover is 38% where DFNC = 0). The cumulative area cover, out of the clear sky, is in green. Error bars represent the standard deviation. Light and dark shaded areas are the TLW extent and effective extent, respectively.

defines every suspected pixel as a cloud (sometimes containing heavy smoke, dust or other high-aerosol concentrations; Methods). Classifying as cloudy the pixels that have a radiative signal that is in between cloudy and clear omits them from the statistics of the twilight zone and is shown to decrease the TWL effect. Moreover, classifying as cloudy the pixels that are non-related to clouds (for example, bright pixels such as bright surface, dust and so on) will attribute values of small DFNC to regions that are actually far from the cloud (that is, have a weak signal). This will decrease the mean values of the real effect. The mean effect for the 6-day global analysis decreased from 0.75 to 0.66 W m^{-2} when we used the strict mask. An additional analysis was carried out for 2 weeks over the Pacific Ocean (latitudes 60° S to 60° N in June 2014), and it shows similar results (that is, effect of 0.84 W m^{-2}; Supplementary Fig. 7).

Implications for atmospheric research

The inherent overlap in radiative properties between clouds with a weak signature (optically thin, or small compared with the detectors' resolution) and other atmospheric or surface features implies that a binary classification will always suffer from errors. No threshold or criteria can perfectly separate clouds from cloud-free areas. Thus, the twilight zone is a natural feature of the cloud field and should be viewed as an additional class. The approach to study and quantify the twilight zone may be dependent on the considered (or utilized) observational dataset. For estimation of the radiative contribution from remote-sensing measurements, the continuum approach in which the average properties are measured as the distance from the nearest cloud or as the mean for the whole field is often useful. In the case of a high-resolution cloud physics study that aims for a process-level understanding, the twilight components should be studied individually. In coarser-scale studies for which cloud fields are parametrized in the sub-grid scale, the twilight could be considered as an additional class (not cloudy or clear sky). Its area coverage and RE can be estimated using the local thermodynamic and aerosol properties.

In this study we show that the TLW RE extends to a distance of ~11 km from detectable clouds, showing an exponential-like decay. More than 90% of the effect is confined to a belt in the range of ~4 km around the clouds. This belt covers more than 60% of the clear sky within the image (Fig. 5b). The averaged radiative forcing inside this confined belt is in the range of 0.6–0.8 W m^{-2}. To put these numbers in perspective, a forcing of ~0.75 W m^{-2} is equivalent to an addition of ~75 ppm CO_2 to the atmospheric column (60% of the increase since the pre-industrial period). Previous studies have shown that 50% of the global so-called clear sky over oceans is located within 5 km of low-level clouds[13,32]. From a climate perspective, this part of the sky is usually overlooked by both cloud and cloud-free applications or treated inaccurately. As an example, clouds correlate well with a humid environment[33–35], and therefore, avoiding near-cloud pixels for water-vapour retrieval implies a bias in the measurements towards a drier atmosphere[36]. A better understanding of the clouds' twilight zone and the representation of its interactions with both longwave and shortwave radiation might reduce some of the high uncertainties caused by clouds in three main aspects:

a. Atmospheric observations: reducing systematic effects in remote-sensing retrievals
b. Cloud and water-vapour feedback: via a better understanding and representation of clouds' mixing with their environment
And most important:
c. CRE: considering the radiative effect of a cloudy region while accounting for both clouds and non-cloudy areas (the twilight zone) can lead to more accurate quantification of CRE and global energy-budget closure

Finally, we reiterate that our radiative estimations present a lower bound of the effect, and we focus here on low-level clouds, which are the warmest type of clouds. Therefore, the overall TLW RE is likely to be higher.

Online content

Any methods, additional references, Nature Research reporting summaries, source data, extended data, supplementary information, acknowledgements, peer review information; details of author contributions and competing interests; and statements of data and code availability are available at https://doi.org/10.1038/s41561-020-0636-8.

Received: 21 August 2019; Accepted: 14 August 2020;
Published online: 21 September 2020

References

1. Myhre, G. et al. in *Climate Change 2013: The Physical Science Basis* (eds Stocker, T. F. et al.) 659–740 (IPCC, Cambridge Univ. Press, 2013).
2. Sherwood, S. C., Bony, S. & Dufresne, J.-L. Spread in model climate sensitivity traced to atmospheric convective mixing. *Nature* **505**, 37–42 (2014).
3. Clement, A. C., Burgman, R. & Norris, J. R. Observational and model evidence for positive low-level cloud feedback. *Science* **325**, 460–464 (2009).
4. Ceppi, P., Brient, F., Zelinka, M. D. & Hartmann, D. L. Cloud feedback mechanisms and their representation in global climate models. *Wiley Interdiscip. Rev. Clim. Change* **8**, e465 (2017).
5. Hartmann, D. L., Ockert-Bell, M. E. & Michelsen, M. L. The effect of cloud type on Earth's energy balance: global analysis. *J. Clim.* **5**, 1281–1304 (1992).
6. Koren, I., Remer, L. A., Altaratz, O., Martins, J. V. & Davidi, A. Aerosol-induced changes of convective cloud anvils produce strong climate warming. *Atmos. Chem. Phys.* **10**, 5001–5010 (2010).
7. Chen, T., Rossow, W. B. & Zhang, Y. Radiative effects of cloud-type variations. *J. Clim.* **13**, 264–286 (2000).
8. Zelinka, M. D., Klein, S. A. & Hartmann, D. L. Computing and partitioning cloud feedbacks using cloud property histograms. Part I: cloud radiative kernels. *J. Clim.* **25**, 3715–3735 (2012).

9. Yue, Q. et al. Observation-based longwave cloud radiative kernels derived from the A-train. *J. Clim.* **29**, 2023–2040 (2016).
10. Calbó, J., Long, C. N., González, J.-A., Augustine, J. & McComiskey, A. The thin border between cloud and aerosol: sensitivity of several ground based observation techniques. *Atmos. Res.* **196**, 248–260 (2017).
11. Koren, I., Remer, L. A., Kaufman, Y. J., Rudich, Y. & Martins, J. V. On the twilight zone between clouds and aerosols. *Geophys. Res. Lett.* **34**, L08805 (2007).
12. Charlson, R. J., Ackerman, A. S., Bender, F. A.-M., Anderson, T. L. & Liu, Z. On the climate forcing consequences of the albedo continuum between cloudy and clear air. *Tellus B* **59**, 715–727 (2007).
13. Bar-Or, R. Z., Altaratz, O. & Koren, I. Global analysis of cloud field coverage and radiative properties, using morphological methods and MODIS observations. *Atmos. Chem. Phys.* **11**, 191–200 (2011).
14. Twohy, C. H., Coakley, J. A. & Tahnk, W. R. Effect of changes in relative humidity on aerosol scattering near clouds. *J. Geophys. Res.* **114**, D05205 (2009).
15. Koren, I., Oreopoulos, L., Feingold, G., Remer, L. A. & Altaratz, O. How small is a small cloud? *Atmos. Chem. Phys.* **8**, 3855–3864 (2008).
16. Hirsch, E., Koren, I., Levin, Z., Altaratz, O. & Agassi, E. On transition-zone water clouds. *Atmos. Chem. Phys.* **14**, 9001–9012 (2014).
17. Leahy, L. V. et al. On the nature and extent of optically thin marine low clouds. *J. Geophys. Res.* **117**, D22201 (2012).
18. Wen, G., Marshak, A., Cahalan, R. F., Remer, L. A. & Kleidman, R. G. 3-D aerosol–cloud radiative interaction observed in collocated MODIS and ASTER images of cumulus cloud fields. *J. Geophys. Res.* **112**, D13204 (2007).
19. Marshak, A., Platnick, S., Várnai, T., Wen, G. & Cahalan, R. F. Impact of three-dimensional radiative effects on satellite retrievals of cloud droplet sizes. *J. Geophys. Res.* **111**, D09207 (2006).
20. Bar-Or, R. Z., Koren, I., Altaratz, O. & Fredj, E. Radiative properties of humidified aerosols in cloudy environment. *Atmos. Res.* **118**, 280–294 (2012).
21. Fuchs, J. & Cermak, J. Where aerosols become clouds—potential for global analysis based on CALIPSO data. *Remote Sens.* **7**, 4178–4190 (2015).
22. Schwarz, K., Cermak, J., Fuchs, J. & Andersen, H. Mapping the twilight zone—what we are missing between clouds and aerosols. *Remote Sens.* **9**, 577 (2017).
23. Brown, O. B. et al. *MODIS Infrared Sea Surface Temperature Algorithm: Algorithm Theoretical Basis Document: Version 2.0* (Univ. of Miami, 1999).
24. Reid, J. S., Hobbs, P. V., Rangno, A. L. & Hegg, D. A. Relationships between cloud droplet effective radius, liquid water content, and droplet concentration for warm clouds in Brazil embedded in biomass smoke. *J. Geophys. Res.* **104**, 6145–6153 (1999).
25. Evans, K. F. The spherical harmonics discrete ordinate method for three-dimensional atmospheric radiative transfer. *J. Atmos. Sci.* **55**, 429–446 (1998).
26. Mätzler, C. *MATLAB functions for Mie Scattering and Absorption* Research Report No. 2002-08 (IAP, 2002).
27. Várnai, T. & Marshak, A. MODIS observations of enhanced clear sky reflectance near clouds. *Geophys. Res. Lett.* **36**, L06807 (2009).
28. Minnett, P. J., Brown, O. B. & Evans, R. H. Sea-surface temperature measurements from the Moderate-Resolution Imaging Spectroradiometer (MODIS) on Aqua and Terra. In *Proc. IEEE International Geoscience and Remote Sensing Symposium* Vol. 7, 4576–4579 (IEEE, 2004).
29. Kilpatrick, K. A. et al. A decade of sea surface temperature from MODIS. *Remote Sens. Environ.* **165**, 27–41 (2015).
30. Platnick, S. et al. The MODIS cloud products: algorithms and examples from Terra. *IEEE Trans. Geosci. Remote Sens.* **41**, 459–473 (2003).
31. Ackerman, S. A. et al. Discriminating clear sky from clouds with MODIS. *J. Geophys. Res.* **103**, 32141–32157 (1998).
32. Várnai, T. & Marshak, A. Analysis of co-located MODIS and CALIPSO observations near clouds. *Atmos. Meas. Tech.* **5**, 389–396 (2012).
33. Perry, K. D. & Hobbs, P. V. Influences of isolated cumulus clouds on the humidity of their surroundings. *J. Atmos. Sci.* **53**, 159–174 (1996).
34. Wang, Y. & Geerts, B. Humidity variations across the edge of trade wind cumuli: observations and dynamical implications. *Atmos. Res.* **97**, 144–156 (2010).
35. Gaffen, D. J. & Elliott, W. P. Column water vapor content in clear and cloudy skies. *J. Clim.* **6**, 2278–2287 (1993).
36. Sohn, B. J., Nakajima, T., Satoh, M. & Jang, H. S. Impact of different definitions of clear-sky flux on the determination of longwave cloud radiative forcing: NICAM simulation results. *Atmos. Chem. Phys.* **10**, 11641–11646 (2010).

Methods

Dataset. The main analysis (6 days of global analysis during 21–23 June 2014 and 21–23 December 2014 at Latitudes 60° S to 60° N) considered 353 scenes of warm cumulus cloud fields over the ocean as measured by MODIS/Aqua in 1 km resolution (level 1B). Another analysis, which focused on the Pacific Ocean, was carried out to confirm the results (181 scenes over the Pacific Ocean, latitudes 60° S to 60° N, 1–15 June 2014). From each granule, we took only pixels that were 10 km away from land, not affected by the ocean glint and had no ice in the background surface. The data were restricted to warm clouds only by using the MODIS cloud products[30], taking only liquid-phase clouds with top temperatures warmer than 275 K. We took a safe distance of 20 km from every detected ice phase pixel and 10 km from uncertain phase to avoid ice clouds' twilight zone. After omitting the pixels that had not met the criteria, each patch (connected pixels) was treated as a cloud field scene and analysed individually, but only if it was larger than 3,500 km^2. To avoid optical complications, we used sensor angles close to nadir of ±15° (ref. [37]). In addition, we used MODIS SST level 3 8-day averages (the best-quality retrievals) at 4 km resolution for the estimation of SST unaffected by clouds, which has an accuracy of 0.05 K (Aqua)[28,29].

Cloud masks. To screen out clouds and calculate the DFNC, we used MODIS's cloud mask product (MYD35) in two different quality assurance levels: cloudy and uncertain (that is, 66–95% clear), represented by flags 00 and 01, respectively. The second cloud mask is a clear-sky conservative mask, meaning that it is used for retrievals of surface properties and atmospheric features (other than clouds, for example, water vapour), and therefore, it defines every suspected pixel as cloudy[31]. This mask defines pixels as cloudy even if they had only 34% probability of being cloudy (note that the two masks agreed on more than 90% of the pixels). Supplementary Fig. 3 shows the differences between the two masks presented in the zoom-in image in Fig. 1c.

Estimation of the radiative effect. The RE was estimated by treating each pixel in the scene as an independent atmospheric column, calculated according to:

$$\mathrm{RE} = F_{\mathrm{sfc}} - F_{\mathrm{TOA}} = \pi \int_{8.4}^{12.2} B_{\lambda,\mathrm{SST}_{8\_\mathrm{day}}}\,\mathrm{d}\lambda - F_{\mathrm{TOA}} \quad (1)$$

where F_{sfc} is the surface flux and F_{TOA} is the flux from the top of the atmosphere. The surface fluxes were obtained by using SST (8-day product) as the temperature in Planck's function ($B_{\lambda,\mathrm{T}}$), and F_{TOA} was obtained using the radiance measured by the satellite. For this, we interpolated MODIS narrow bands into broadband and converted the radiance to flux, taking a conservative approach, which gave the lower bound to the effect (section 5 of the Supplementary Information). Estimation of the uncertainty of the calculated RE was done with a Monte Carlo error propagation using the uncertainties of MODIS's sensors and level 2 SST product, combined with the analysed uncertainty of the interpolation (section 6 of the Supplementary Information). The integral limits for the total fluxes were set according to the response function of the MODIS sensors, and the RE of all pixels was binned and averaged according to DFNC (Fig. 4a). The TLW extent was defined (along the decay curve) as the point where the values were close to saturation, where the derivative was close to zero and the standard deviation remained small until the end of the x axis (largest DFNC). All DFNC bins that were farther away from the TLW extent were averaged to give the atmospheric background RE ($\mathrm{RE}_{\mathrm{clr}}$). The TLW RE of each DFNC bin was calculated by removing the background effect (subtracting $\mathrm{RE}_{\mathrm{clr}}$ from each bin's value). The total TLW RE of the scene was obtained by summing all DFNC bins while weighting each one by its areal coverage of the domain's clear sky:

$$\mathrm{TLW\ RE} = \sum\nolimits_i (\mathrm{RE}_i - \mathrm{RE}_{\mathrm{clr}}) \times \frac{n_i}{N_{\mathrm{clr}}} \quad (2)$$

where i is the DFNC bin index, N_{clr} is the number of clear-sky pixels and n_i is the number of pixels in the DFNC bin, such that $\frac{n_i}{N_{\mathrm{clr}}}$ is the areal coverage of the pixels located at a certain distance from the cloud, according to bin i.

Theoretical aspects of the longwave twilight zone. The investigation of the longwave radiation transfer characteristics in the cloud's twilight zone and examination of the different components were performed using Mie theory calculations[26] and a radiative transfer model (SHDOM)[25] and are presented in Supplementary Information section 1.

Data availability

The MODIS level 2 products—cloud mask, cloud properties and level 1B raw data—are available from the Atmosphere Archive and Distribution System (LAADS) Distributed Active Archive Center (DAAC), https://ladsweb.modaps.eosdis.nasa.gov/. The MODIS sea surface temperature products of levels 2 and 3 are available from Ocean Color Web, https://oceancolor.gsfc.nasa.gov/. Source data are provided with this paper.

Code availability

The radiation transfer codes are open access; SHDOM is available at http://coloradolinux.com/shdom/; SBDART is available at https://github.com/paulricchiazzi/SBDART.

References

37. Loeb, N. G., Kato, S., Loukachine, K. & Manalo-Smith, N. Angular distribution models for top-of-atmosphere radiative flux estimation from the clouds and the Earth's radiant energy system instrument on the *Terra* satellite. Part I: methodology. *J. Atmos. Ocean. Technol.* **22**, 338–351 (2005).

Acknowledgements

This project has received funding from the European Research Council (ERC) under the European Union's Horizon 2020 research and innovation programme (CloudCT, grant agreement No. 810370). A.B.K. is supported in part by NSF AGS-1639868.

Author contributions

E.E. and I.K. jointly conceived the principal idea. E.E. carried out the analysis. E.E., I.K., O.A., A.B.K. and A.R. discussed results and wrote the paper.

Competing interests

The authors declare no competing interests.

Additional information

Supplementary information is available for this paper at https://doi.org/10.1038/s41561-020-0636-8.

Correspondence and requests for materials should be addressed to I.K.

Peer review information Primary Handling Editors: Tamara Goldin; Heike Langenberg; Tom Richardson.

Reprints and permissions information is available at www.nature.com/reprints.